JCI The Journal of Clinical Investigation

Dysfunction of parvalbumin neurons in the cerebellar nuclei produces an action tremor

Mu Zhou, … , Wei Xu, Thomas C. Sudhof

J Clin Invest. 2020. https://doi.org/10.1172/JCI135802.

Research In-Press Preview **Neuroscience**

Graphical abstract

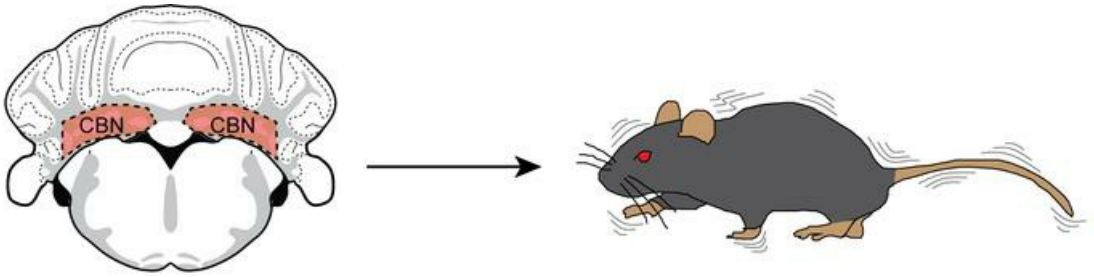

Deletion of synaptotagmin 2 from parvalbumin neurons in the cerebellar nuclei (CBN) results in action tremor of mice.

Dysfunction of parvalbumin neurons in the cerebellar nuclei produces an action tremor

Mu Zhou,[1] Maxwell D. Melin,[1] Wei Xu,[1] and Thomas C. Südhof[1,2]

[1]Department of Molecular and Cellular Physiology, Stanford University School of Medicine, 265 Campus Drive, Stanford, CA 94305, USA.

[2]Howard Hughes Medical Institute, Stanford University School of Medicine, 265 Campus Drive, Stanford, CA 94305, USA.

Maxwell Melin's present address: UCLA-Caltech MSTP program, Los Angeles, California 90095, USA.

Wei Xu's present address: Department of Neuroscience, UT Southwestern Medical Center, Dallas, Texas 75235, USA.

Address correspondence to: Mu Zhou, 265 Campus Drive, Stanford, CA 94305, USA**.** Phone**:** +1-6507211421; Email: muzhou@stanford.edu

Conflict of interest: The authors declared no conflict of interest.

Abstract

Essential tremor is a common brain disorder affecting millions of people, yet the neuronal mechanisms underlying this prevalent disease remain elusive. Here, we show that conditional deletion of synaptotagmin-2, the fastest Ca^{2+}-sensor for synaptic neurotransmitter release, from parvalbumin neurons in mice causes an action tremor syndrome resembling the core symptom of essential tremor patients. Combining brain region-specific and cell type-specific genetic manipulation methods, we found that deletion of synaptotagmin-2 from excitatory parvalbumin-positive neurons in cerebellar nuclei was sufficient to generate an action tremor. The synaptotagmin-2 deletion converted synchronous into asynchronous neurotransmitter release in projections from cerebellar nuclei neurons onto gigantocellular reticular nucleus neurons, which might produce an action tremor by causing signal oscillations during movement. The tremor was rescued by completely blocking synaptic transmission with tetanus toxin in cerebellar nuclei, which also reversed the tremor phenotype in the traditional harmaline-induced essential tremor model. Using a promising animal model for action tremor, our results thus characterize a synaptic circuit mechanism that may underlie the prevalent essential tremor disorder.

Introduction

Essential tremor is the most common movement disorder of human patients (1). Clinically, essential tremor is characterized by a 4-12 Hz action tremor (2) that affects different body parts, making basic daily activities difficult if not impossible in severe cases. While no consensus has been reached on its exact prevalence, surveys show that the disease is present in 4% of individuals aged 40 and up (3). Essential tremor prevalence increases with age, such that up to 14% of people aged 65 and above exhibit essential tremor (4). Despite its widespread presence, our understanding of essential tremor's biological mechanisms remains very limited (5), and few therapeutic options are available.

Studies of the etiology of essential tremor traditionally focused on the inferior olive (6-8). In an animal model of essential tremor induced by intraperitoneal (i.p.) injections of harmaline, rhythmic burst-firing was detected in inferior olive neurons and an action tremor was induced that exhibited the same frequency as the rhythmic firing in inferior olive neurons (6). Although these findings were promising, decades of clinical research found little evidence for a dysfunction or for pathological changes in the inferior olive in essential tremor patients (5). More recently, postmortem analyses and advanced neuroimaging techniques have identified pathological changes in the cerebellum, including Purkinje cells, basket cells and the cerebellar nuclei (CBN) in essential tremor patients (9-13). In particular, degeneration of Purkinje cells has become a widely believed hypothesis to account for essential tremor (5). Yet, the data so far are correlative. There is no evidence to show the causality between cerebellar pathologies and essential tremor symptoms. More importantly, the physiological basis by which cerebellar dysfunction might lead to essential tremor remains unknown.

A major obstacle to a better understanding of the etiology of essential tremor is the lack of a reliable genetic animal model (14-16). The traditional harmaline-induced essential tremor model is useful for the preclinical testing of anti-tremor drugs. However, this model has limited value for translational research since its tremor symptoms spontaneously resolve in a few hours (6, 8). Recently, several genetic tremor animal models were described (15-18) that provided critical insights into the neural mechanisms of essential tremor. Nevertheless, these genetic models have limitations because they either exhibit non-specific action tremor or produce a much higher tremor frequency than observed in essential tremor patients.

Synaptotagmin-2 (Syt2) is an ultrafast Ca^{2+}-sensor for fast neurotransmitter release (19-21). We initially crossed Syt2 conditional knockout ($Syt2^{fl/fl}$, 'fl' short for 'floxed') mice with parvalbumin-Cre (PV^{cre}) driver mice in order to study the functional roles of Syt2 at the calyx of Held synapse (21) and at cortical inhibitory synapses. Unexpectedly, we found that PV^{cre}:$Syt2^{fl/fl}$ mice exhibited a robust action tremor phenotype without other obvious behavioral abnormalities. This surprising discovery provided us a unique opportunity to examine the circuit components and pathological synaptic release properties that can underlie action tremor, the core symptom of the prevalent essential tremor disorder in human patients.

Combining region, cell type and projection-specific deletions of Syt2, we here identify the dysfunction of excitatory PV-positive (PV^{+}) neurons in the CBN that project to neurons in the brainstem as the cause of action tremor. We determined that in PV^{cre}-$Syt2^{fl/fl}$ mice, fast synchronous synaptic neurotransmitter release in this cerebellum → brainstem circuit was converted into asynchronous neurotransmitter release, which then led to action tremor. We also found that blocking synaptic transmission in CBN reversed the action tremor phenotype in PV^{cre}-$Syt2^{fl/fl}$ mice, and that this rescue approach was also effective for harmaline-induced action

tremor, the traditional animal model of essential tremor. Based on these data, we propose a conceptual framework to explain how temporally delayed synaptic transmission in the cerebellum → brainstem pathway could generate an action tremor. In summary, our study validates a promising genetic mouse model for action tremor and defines critical circuit components that generate such a tremor. The circuit components and synaptic defects we identified may provide significant insights into the etiology and therapeutic intervention of the wide spread essential tremor brain disorder.

Results

PV^{cre}-$Syt2^{fl}$ mice are a promising animal model for action tremor

By crossing $PV^{cre/cre}$:$Syt2^{fl/+}$ mice with $Syt2^{fl/fl}$ mice, we generated mice with a deletion of Syt2 in PV neurons ($PV^{cre/+}$:$Syt2^{fl/fl}$, referred to as PV^{cre}-$Syt2^{fl}$) that exhibit a robust action tremor phenotype, while their heterozygous littermates ($PV^{cre/+}$:$Syt2^{fl/+}$, referred to as PV^{cre}-$Syt2^{wt}$ or control) were normal (Supplementary Movie 1 and 2). Immunostaining confirmed the deletion of Syt2 from PV^{+} synapses (Supplementary Figure 1). To quantify the action tremor, we used a 28 x 28 cm force-plate actometer that was designed to measure the whole body weight at 100 Hz (22). PV^{cre}-$Syt2^{fl}$ mice exhibited an obvious tremor with a ~10 Hz rhythm, whereas their littermate PV^{cre}-$Syt2^{wt}$ controls did not (Figure 1, A and B). For each mouse, we plotted the averaged power spectrum and defined a "tremor index" as the summation of power in the 9-12 Hz range, using the power in the 3-6 Hz range as the baseline (Figure 1C). To cross-validate this tremor quantification method, we also directly measured the tremor amplitude of PV^{cre}-$Syt2^{fl}$ and control mice using video tracking methods while measuring at the same time their behavior on the force plate. Using a high-speed camera and video tracking software, the detailed movements of mice were recorded and band-pass filtered (9-12 Hz) to calculate the tremor amplitude (Supplementary Figure 2). This approach confirmed the tremor phenotype in PV^{cre}-$Syt2^{fl}$ mice and validated the usage of the force-plate actometer to quantify the tremor phenotype (Figure 1D).

The tremor of PV^{cre}-$Syt2^{fl}$ mice manifested at the time of weaning and became increasingly stronger as the mice grew older, as documented by force plate quantifications as a function of age (Figure 1, E and F). Importantly, the observed age-dependent increase of tremor strength was not due to the increase in body size, as shown by plotting the tremor index

normalized to the body weight (Supplementary Figure 3A). This age-dependent pattern of increasing tremor is consistent with clinical observations (2). Besides the tremor phenotype, PV^{cre}-$Syt2^{fl}$ mice were grossly normal. Their body weight was similar to that of littermate controls (Supplementary Figure 3B). They were fertile and exhibited a normal life span, as followed up to 1.3 years, the oldest age we monitored. PV^{cre}-$Syt2^{fl}$ mice likely have normal cognitive abilities as suggested by results from spontaneous alternating Y maze (Supplementary Figure 3C), novel object recognition (Supplementary Figure 3D) and fear conditioning assays (Supplementary Figure 3E). PV^{cre}-$Syt2^{fl}$ mice did, however, show a significant deficit in the rotarod test (Supplementary Figure 3F), which is not surprising given their striking action tremor.

We next tested whether ethanol, which had been shown to temporarily alleviate essential tremor symptoms in human patients (2, 23), had a similar effect in PV^{cre}-$Syt2^{fl}$ mice. A single subcutaneous (s.c.) injection of 2.5 g/kg ethanol dramatically but temporarily suppressed the tremor of PV^{cre}-$Syt2^{fl}$ mice (Figure 1G and Supplementary Figure 3G). Importantly, the suppression of the tremor by ethanol could not be explained by the reduction in locomotion (Supplementary Figure 3, H and I). Moreover, we noticed that the PV^{cre}-$Syt2^{fl}$ mice had little or no tremor when they were at rest and not moving (Supplementary Movie 2 and 3), suggesting that they have an action tremor phenotype. We quantified this aspect by measuring the moving speed and the instantaneous tremor index of PV^{cre}-$Syt2^{fl}$ mice at the same time (Figure 1H). Although mice usually continuously explored the novel environment and had few quiescent episodes, their action tremor phenotype became obvious when we selected all quiescent epochs of longer than 3 sec and examined the tremor index before, during and after these quiescent episodes (Figure 1I). Clearly, the tremor decreased during a mouse's quiescent period. The

action tremor phenotype of PV^{cre}-$Syt2^{fl}$ mice was further illustrated in fear conditioning assays, during which PV^{cre}-$Syt2^{fl}$ mice substantially froze to contextual cues (Supplementary Movie 4), strongly suggesting lack of a resting tremor. Together, these results indicate that PV^{cre}-$Syt2^{fl}$ mice are a reliable genetic animal model for action tremor and a promising candidate to model the human essential tremor disorder (Table 1).

Syt2 deletion from the cerebellum is sufficient to generate an action tremor

To identify the brain region that is responsible for generating the action tremor in PV^{cre}-$Syt2^{fl}$ mice, we first compared the Syt2 expression levels in PV^{cre} and PV^{cre}-$Syt2^{fl}$ mice across the entire brain (Figure 2, A and B, and Supplementary Figure 4). The PV^{cre}-induced reduction of Syt2 signals was obvious in the cortex, hippocampus and cerebellum (Figure 2, A and B). Since the reduction of Syt2 signals was most dramatic in cortical areas, likely due to the co-localization of Syt2 and PV expression (24), we analyzed the effect of the Syt2 deletion on inhibitory synaptic responses in the medial prefrontal cortex (mPFC) using whole-cell patch-clamp recordings in acute slices. We tested the change of spontaneous inhibitory postsynaptic currents (sIPSCs) by injecting adeno-associated viruses (AAVs) expressing syn-EGFP-Cre unilaterally in the mPFC of $Syt2^{fl/fl}$ mice and recording sIPSCs from pyramidal neurons on either the GFP or the non-GFP side. Surprisingly, both the frequency and amplitude of recorded sIPSCs were normal on the GFP side, suggesting that Syt2 knockout does not change sIPSCs in the cortex (Figure 2, C and D). We further recorded optogenetically evoked IPSCs by expressing DIO-CHiEF-tdTomato unilaterally in the mPFC of PV^{cre}-$Syt2^{fl}$ and control mice. 1 ms, 45 Hz laser-evoked IPSCs were also normal in PV^{cre}-$Syt2^{fl}$ slices (Figure 2, E and F). These results suggest that synaptic release by cortical PV^{+} neurons is not affected by the Syt2 deletion, potentially due

to the compensatory effect of synaptotagmin-1 (25), which could also explain the lack of other striking phenotypes besides tremor in PV^{cre}-$Syt2^{fl}$ mice.

Next, we employed a more direct approach to delete Syt2 from different brain regions, and tried to identify the specific brain area in which the Syt2 deletion is sufficient to generate an action tremor. We tested four candidate brain areas implicated in motor behaviors for this purpose: the motor cortex, basal ganglia, thalamus and cerebellum. The motor cortex, including the primary and secondary motor cortex, provides command signals for voluntary movements. The basal ganglia are involved in movement initiation, and have been hypothesized to mediate the resting tremor that is a key symptom of Parkinson's disease. The thalamus includes relay centers for motor pathways, and the ventral intermediate nucleus of thalamus is targeted by deep brain stimulation (DBS) to treat essential tremor (26-28). The cerebellum plays a critical role in fine motor control, and pathological studies have detected cerebellar degeneration as a hallmark of essential tremor (5). Strikingly, removing Syt2 expression from the motor cortex, basal ganglia or thalamus did not induce an action tremor (Supplementary Figure 5), whereas removing Syt2 from the cerebellum replicated the action tremor observed in PV^{cre}-$Syt2^{fl}$ mice (Figure 3, A-C; Supplementary Figure 5E; Supplementary Movie 5). These results indicate that removing Syt2 from neurons in the cerebellum is sufficient to generate an action tremor.

Syt2 deletion from PV^{+} neurons in CBN is sufficient to generate an action tremor

To pinpoint the cell types in the cerebellum that generate the action tremor in PV^{cre}-$Syt2^{fl}$ mice, we took advantage of multiple Cre mouse lines that target different PV^{+} cell types in the cerebellum (ref 29, Table 2 and Supplementary Figure 6, A and B). We first crossed $Syt2^{fl/fl}$ mice with $L7^{cre}$ mice, which express Cre recombinase exclusively in Purkinje cells in the cerebellar

cortex (Supplementary Figure 6, A and B). Degeneration of Purkinje cells has been hypothesized to be the cause of essential tremor (5). However, $L7^{cre}$-$Syt2^{fl}$ mice exhibited no action tremor (Figure 4, A and C). Next, we crossed $Syt2^{fl/fl}$ mice with $Prkcd^{cre}$ mice (30), which express Cre recombinase in the molecular layer inhibitory neurons and in some Purkinje cells in the cerebellar cortex (ref 31 and Supplementary Figure 6, A and B). $Prkcd^{cre}$-$Syt2^{fl}$ mice were also normal and had no tremor phenotype (Figure 4C and Supplementary Figure 6C).

To test the roles of neurons in the CBN, we crossed $Syt2^{fl/fl}$ mice with either $Vglut2^{cre}$ or $Gad2^{cre}$ mice, which express Cre recombinase in excitatory and inhibitory neurons, respectively (Supplementary Figure 6, A and B). Surprisingly, $Vglut2^{cre}$-$Syt2^{fl}$ mice exhibited a robust tremor phenotype, whereas $Gad2^{cre}$ mice did not (Figure 4, B and C, and Supplementary Figure 6D). Besides the tremor phenotype, $Vglut2^{cre}$-$Syt2^{fl}$ mice also had a significantly reduced body weight (Supplementary Figure 6E), presumably due to knockout of Syt2 from Vglut2 positive excitatory neurons in brain regions other than the CBN that are not targeted by the PV^{cre} driver line. Since at least in cortical areas, PV^{+} neurons are primarily inhibitory (32), we further crossed PV^{cre} mice with a nucleus-localized tdTomato reporter line (Ai75) and immuno-stained for Vglut2 in the CBN. Indeed, the majority of PV^{+} neurons in the CBN co-localized with $Vglut2^{+}$ neurons, indicating that PV^{+} neurons in the CBN are mostly glutamatergic (Figure 4D).

Both PV^{cre} and $Vglut2^{cre}$ mice express Cre in many other brain regions outside the cerebellum. Therefore we further tested whether removing Syt2 from the CBN alone is sufficient to generate an action tremor. Indeed, bilaterally injecting AAVs expressing Cre into the CBN of $Syt2^{fl/fl}$ mice induced an action tremor with the same frequency range as observed in PV^{cre}-$Syt2^{fl}$ mice (Figure 4, E and F), whereas expressing Cre in either the medial or lateral cerebellar cortex of $Syt2^{fl/fl}$ mice failed to replicate the tremor (Figure 4F and Supplementary Figure 6, F and G).

Furthermore, the age-dependent tremor progression of PV^{cre}-$Syt2^{fl}$ mice was significantly rescued by overexpression of Syt2 in CBN (Figure 4, G and H, and Supplementary Figure 6, H and I). Together, these results indicate that the deletion of Syt2 from CBN is sufficient to generate an action tremor.

Loss of fast synchronous neurotransmitter release at CBN → GRN synapses may induce the action tremor

To identify the downstream targets of PV^{+} neurons in the CBN that generate the action tremor, we injected AAVs expressing Cre-dependent (DIO-) mCherry into the CBN of PV^{cre} mice. Three weeks later, robust mCherry signals were observed in the thalamus (Ventral anterior-lateral complex of the thalamus, VAL; Ventral medial nucleus of the thalamus, VM), the midbrain (Red nucleus; Midbrain reticular nucleus; Periaqueductal gray) and the brainstem (Gigantocellular reticular nucleus, GRN; Parvicellular reticular nucleus; Vestibular nuclei; Figure 5A). Among these brain regions, the VAL and VM may be analogous to the human ventral intermediate nucleus of the thalamus, which has been targeted for DBS treatment (26-28). The red nucleus and VAL were previously proposed to constitute an "essential tremor pathway" outside of the cerebellum (12). Moreover, the GRN has been shown to directly innervate motor neurons in the spinal cord and therefore is in a good position to control fine motor movement (33, 34). We also performed more restricted injections of AAVs expressing DIO-mCherry into each individual nucleus of the CBN (Fastigial nucleus; Interposed nucleus; Dentate nucleus; Supplementary Figure 7, A-C), and found that while all three nuclei project to the brainstem, the midbrain and the thalamus in general, there are some differences. For example, mainly the fastigial nucleus and dentate nucleus project to the GRN (Supplementary Figure 7, A-C). Using retrograde

tracing, we further confirmed that GRN neurons received robust inputs from the fastigial nucleus and dentate nucleus (Supplementary Figure 7, D and E).

To determine whether the same group of CBN neurons project to the GRN and to more rostral brain structures (red nucleus and VAL/VM), we injected retro-AAVs encoding mCherry into the GRN and retro-AAVs encoding GFP into either the red nucleus or the VAL/VM (Supplementary Figure 8, A and C). Subsequent imaging of labeled CBN neurons suggested that distinct CBN neurons project to the GRN and to red nucleus or VAL/VM (Supplementary Figure 8, B and D). To test the roles of different CBN projections in action tremor, we bilaterally injected AAVs expressing wheat germ agglutinin-conjugated Cre (WGA-Cre) into the VAL/VM, red nucleus or GRN of $Syt2^{fl/fl}$ mice that had been crossed with Cre-dependent EYFP reporter mice (Ai3; Supplementary Figure 8, E and F). In this injection paradigm, WGA-Cre was retrogradely transported to presynaptic targets (35, 36), including the CBN, mediating the knockout of Syt2. We found that expression of WGA-Cre in the VAL/VM and red nucleus did not induce tremor (Supplementary Figure 8, E-I). Expression of WGA-Cre in the GRN severely impaired mice, necessitating euthanasia after about one week and preventing analysis of their tremor phenotype. This issue is most likely due to the WGA-Cre induced deletion of Syt2 in the numerous brainstem neurons that project to the GRN (Supplementary Figure 7E), as suggested by the substantial endogenous Syt2 expression in the brainstem and the early lethality of constitutive Syt2 knockout mice (19).

To overcome this limitation and test the roles of CBN neurons projecting to the GRN, we adapted an intersectional method that deletes Syt2 in a pathway-specific manner (Figure 5B). Specifically, we used Syt2-Ai3 mice to inject retro-AAVs encoding flippase into each of the three downstream candidate target nuclei, including the GRN, and regular AAVs expressing

flippase-dependent Cre recombinase (Frt-Cre) into the CBN (Figure 5, B and C). The results showed that removing Syt2 only from CBN neurons projecting to the GRN was sufficient to generate an action tremor (Figure 5, B-E).

To further identify the changes in synaptic neurotransmitter release produced by the knockout of Syt2, we expressed channelrhodopsin in the CBN of PV^{cre}-$Syt2^{fl}$ or PV^{cre}-$Syt2^{wt}$ mice, and recorded synaptic responses from GRN neurons in acute slices using whole-cell voltage-clamp recordings (Figure 6A). We found that in PV^{cre}-$Syt2^{fl}$ slices, the frequency of spontaneous excitatory postsynaptic currents (sEPSCs), which are largely equivalent to miniature EPSCs (mEPSCs), was significantly increased, while the amplitude of sEPSCs was unchanged (Figure 6, B and C). Increases in mEPSC frequency are a typical phenotype induced by deletion of fast synaptotagmins (21). We next stimulated synaptic inputs to the GRN using blue laser light at 50 Hz, and observed that fast synchronous neurotransmitter release was abolished in some of the GRN neurons recorded, whereas asynchronous neurotransmitter release appeared to be enhanced (Figure 6, D and E, and Supplementary Figure 8J). Moreover, we applied rabies tracing to label CBN neurons projecting to GRN. Imaging results suggested that there are no obvious morphological difference between CBN neurons in PV^{cre}-$Syt2^{fl}$ and PV^{cre}-$Syt2^{wt}$ mice (Supplementary Figure 8, K-M). Together, these results suggest that the deletion of Syt2 from CBN neurons causes a loss of fast synchronous but not slower forms of neurotransmitter release, suggesting that a shift in the pattern of evoked neurotransmitter release in CBN → GRN synapses may be the cause of the action tremor observed in PV^{cre}-$Syt2^{fl}$ mice.

Blocking neurotransmitter release in CBN neurons rescues the action tremor of PV^{cre}-$Syt2^{fl}$ mice and of harmaline-injected mice

To test whether the remaining asynchronous neurotransmitter release at CBN → GRN synapses in PV^{cre}-$Syt2^{fl}$ mice induces the action tremor, we expressed Cre-dependent tetanus toxin (DIO-TetTox) in CBN neurons of PV^{cre}-$Syt2^{fl}$ mice, which will block all synaptic release from PV^{+} neurons in the CBN (ref 37 and Figure 7A). Surprisingly, TetTox expression rescued instead of aggravating the age-dependent action tremor in PV^{cre}-$Syt2^{fl}$ mice (Figure 7, B and C, and Supplementary Figure 9, A and B), suggesting that the action tremor of PV^{cre}-$Syt2^{fl}$ mice is generated by the malfunction of CBN → GRN synapses, instead of a simple loss-of-function at these synapses. A detailed spectral analysis showed that after TetTox expression, the 9-12 Hz action tremor was largely gone, whereas a ~8 Hz tremor became manifest (Figure 7B and Supplementary Figure 9C). This TetTox-induced lower frequency tremor could be explained by two possible mechanisms, a frequency shift of the original 9-12 Hz action tremor, or a ~ 8 Hz tremor generated de-novo. To understand the nature of this ~8 Hz tremor, we expressed DIO-TetTox in the CBN of PV^{cre} mice (Supplementary Figure 9D), which did not exhibit visible tremor. Interestingly, completely blocking the synaptic release in CBN PV^{+} neurons in PV^{cre} mice induced tremor at ~8 Hz (Supplementary Figure 9, E and F), the same frequency range as the physiological tremor in PV^{cre} mice (Supplementary Figure 9, E and G). This result suggests that the remaining ~8 Hz tremor after blocking all synaptic release from PV^{+} neurons in the CBN neurons of PV^{cre}-$Syt2^{fl}$ mice is not due to a frequency shift of the 9-12 Hz action tremor.

Next we tested whether completely blocking synaptic transmission in CBN PV^{+} neurons (Figure 8A) could also rescue the tremor phenotype in the harmaline-induced essential tremor model, which exhibits an 11-14 Hz action tremor (Figure 8B and Supplementary Figure 10, A and B). Indeed, TetTox-injected PV^{cre} mice failed to exhibit the typical 11-14 Hz action tremor normally induced by harmaline injections (Figure 8, C and D), although a reduction of

locomotion partially contributed to this phenotype (Supplementary Figure 10C). Furthermore, we selectively blocked synaptic transmission in CBN PV^+ neurons that project to the GRN or VAL/VM (Figure 8, E and F). The harmaline-induced 11-14 Hz tremor was completely eliminated after blocking the CBN → GRN pathway, but not after blocking the CBN → VAL/VM pathway (Figure 8, G-I). Again, the reduction of locomotion partially contributed to these reductions in harmaline-induced action tremor (Supplementary Figure 10, D-F). Together, these results suggest that an increase in asynchronous neurotransmitter release at CBN → GRN synapses may be a general mechanism of action tremors observed in different animal models.

Discussion

In this study, we generated a mouse model that exhibits an action tremor with properties resembling the action tremor observed in the human essential tremor disorder, suggesting that the mouse model we describe might help to gain insight into the etiology of the human essential tremor. There are three criteria for a valid animal disease model: face validity, predictive validity and target validity (38). We found that PV^{cre}-$Syt2^{fl}$ mice exhibited a 9-12 Hz action tremor that became progressively worse with age, replicating the major symptoms of essential tremor patients (face validity). The action tremor of PV^{cre}-$Syt2^{fl}$ mice was temporarily suppressed by ethanol, similar to the effect of alcohol in essential tremor patients (predictive validity). Moreover, we identified synapses formed by neurons in the CBN on GRN neurons in the brainstem as the cause of the action tremor in PV^{cre}-$Syt2^{fl}$ mice, coinciding with the cerebellum's proposed tremorogenic role in human essential tremor patients (target validity). Together, these data suggest that PV^{cre}-$Syt2^{fl}$ mice add significantly to existing animal models (14-18) to study the pathophysiology of essential tremor and to generate new ideas for therapeutic intervention.

Taking advantage of our PV^{cre}-$Syt2^{fl}$ mouse model, we observed that dysfunction of excitatory PV^{+} neurons in CBN is sufficient to generate the action tremor. Previously, GABAergic Purkinje cells in the cerebellar cortex were proposed to play a critical role in essential tremor (5). Since glutamatergic neurons in CBN are the major output neurons of the cerebellum and receive direct inputs from Purkinje cells, our results thus may have identified a key circuit component of essential tremor. In fact, some previous studies in humans and monkeys have suggested a role for CBN in essential tremor (39-41).

Using an intersectional genetic manipulation, we also demonstrated that the projection from CBN to the GRN in the brainstem, but not the projection to the thalamus, is critical for

generating the action tremor. Traditionally, the CBN → thalamus → cortex pathway was proposed to be the "tremor pathway" (12), based on the finding that deep brain stimulation of the ventral intermediate nucleus of the thalamus could suppress the essential tremor in patients (26-28). There are two possible explanations for our findings. First, PV^{cre}-$Syt2^{fl}$ mice may only recapitulate the mechanisms of a subgroup of essential tremor patients, of whom the disease mechanism is different from the majority. Second, the major function of CBN → thalamus pathway may be to suppress instead of generating the action tremor. Our tracing results show that neurons in the fastigial and dentate nuclei of the CBN project to the GRN (Supplementary Figure 7, A-E), suggesting that these neurons are responsible for inducing the action tremor. Indeed, previous studies showed that cooling the dentate nucleus could induce an action tremor (42, 43). CBN neurons projecting to the red nucleus and VAL/VM are largely distinct from GRN-projecting neurons (Supplementary Figure 8, A-D). We speculate that these CBN → thalamus projection neurons could be responsible for suppressing action tremor. From a clinical perspective, in the future it will be important to apply advanced neuroimaging techniques to record whether activities in the brainstem regions are correlated with the action tremor of essential tremor patients. It will also be illuminating to test whether directly intervening with the CBN → GRN pathway (with DBS for example) would be a better treatment for essential tremor.

The synaptic deficits we observed at the CBN → GRN synapses (Figure 6, B-E) are consistent with previous studies of the role of synaptotagmins in clamping and mediating fast synchronous neurotransmitter release (20, 21, 44, 45). These synaptic changes correlate well with the tremor and provide interesting insights into the roles of the cerebellum in action tremor. In our working model (Figure 9A), we propose that the cerebellum receives a copy of the motor command and another copy of the motor execution feedback on a moment-by-moment basis. If

these two signals are not perfectly matched, the cerebellar circuits will calculate the real-time "correction" signal needed to adjust and smoothen the ongoing movement (46). This hypothesized "correction" signal likely flows from the glutamatergic PV^+ neurons in the CBN to GRN neurons, which are directly connected to motor neurons in the spinal cord (33, 34), thereby adjusting the motor command signals in real time. If Syt2 is removed from glutamatergic neurons in the CBN, this "correction" signal becomes temporally delayed and causes oscillations of the motor command signals, thereby inducing tremor (Figure 9B). Since this delayed "correction" signal only applies to the movement phase, the resulting tremor would be specifically an action tremor, as opposed to a resting tremor. Completely abolishing this pathologically delayed "correction" signal, as by TetTox treatment, removes the oscillation of the motor command and blocks the 9-12 Hz action tremor (Figure 9B). In general, our working model is consistent with the previous understanding of the role of the cerebellum in motor learning (47). Future studies will be needed to identify the neural circuits that transmit the motor command and execution feedback signals into the cerebellum, to characterize the local cerebellar circuit computing the "correction" signal, and to determine how oscillations are generated in downstream targets and how the frequency and amplitude of the resulting tremor are determined.

In this study, we used Syt2 as a "molecular tool" to identify the circuit components and synaptic defects underlying an action tremor. Given the wide distribution of PV^+ cells in the nervous system and the critical role of Syt2 as a fast Ca^{2+}-sensor for neurotransmitter release (19, 20, 45, 48), it is somewhat unexpected that PV^{cre}-$Syt2^{fl}$ mice display a specific action tremor phenotype without exhibiting other dramatic behavioral defects (Supplementary Figure 3, B-E). We think there are two reasons for this phenotypic specificity. First, the function of Syt2 could be compensated by other synaptotagmin isoforms that mediate fast and intermediate synchronous

neurotransmitter release (25, 37), as supported by our recording results in the cortex (Figure 2, C-F). Second, many cells expressing Syt2 as the only fast Ca^{2+}-sensor are PV-negative, as supported by the lethality in Syt2 constitutive KO mice (19) and the dramatic weight loss in $Vglut2^{cre}$-$Syt2^{fl}$ mice (Supplementary Figure 6E). Therefore, PV^{cre}-$Syt2^{fl}$ mice serendipitously target, among others, a specific population of PV^{+} neurons in the CBN that use Syt2 as the only fast Ca^{2+}-sensor and play critical roles in action tremor.

A limitation to our study is that Syt2 has not been shown as an essential tremor risk gene. Although the genetics of essential tremor is still poorly understood (49, 50), we don't think Syt2 will be identified as a risk gene for essential tremor patients, because of the lethality in Syt2 constitutive KO mice, which reveal its central importance in brain function. Nevertheless, we found that PV^{cre}-$Syt2^{fl}$ mice reproduced the major symptoms of essential tremor patients. The critical neural pathway and synaptic release defect we identified using this mouse model are likely downstream of the initial genetic cause and are probably shared by different animal models and human patients of essential tremor. Indeed, we found that blocking the abnormal neurotransmitter release in CBN PV^{+} neurons with TetTox could also rescue the action tremor of harmaline-injected mice (Figure 8, C and D). Our data thus suggest that PV^{cre}-$Syt2^{fl}$ mice are a reliable action tremor model that promises to be of use for studying the etiology of essential tremor and for developing therapeutic interventions in essential tremor patients.

Methods

Animals: Syt2$^{fl/fl}$ mice were designed to have Syt2 exon 2 flanked by loxP sites and were generated at Janelia Farm gene targeting and transgenics center (21). They were backcrossed to C57/Bl6J wildtype mice for at least 7 times. C57BL/6J, PV^{cre}, L7^{cre}, Vglut2^{cre}, GAD2^{cre}, Ai3, Ai14 and Ai75 transgenic mice were purchased from Jaxson lab. Prkcd^{cre} mice were generously provided by Dr. David Anderson's laboratory at Caltech. Syt2$^{fl/fl}$ mice were crossed with each different Cre driver line two generations to generate Driver$^{cre/cre}$:Syt2$^{fl/+}$ mice. These mice were then crossed with Syt2$^{fl/fl}$ mice to generate littermate control (Driver$^{cre/+}$:Syt2$^{fl/+}$) and knockout mice (Driver$^{cre/+}$:Syt2$^{fl/fl}$) for experiments. The littermate control mice were used in all related experiments except for results shown in Figure 2, A and B, and Supplementary Figure 4, in which PV^{cre} mice were used as control. Genotyping was performed by Transnetyx (Cordova, TN). Mice were group housed (maximum 5 mice in a cage) on a 12 hours light/dark cycle (7 am to 7 pm, light) with food and water freely available. Roughly equal number of males and females were used for all experiments.

Vector construction and AAV preparation: AAV CAG-Cre-GFP and AAV CAG-GFP-2A-Syt2 were packaged with AAV-DJ capsids for high efficiency in vivo neuronal infection. Virus was prepared with a procedure as previously described (36). Briefly, the CAG-Cre-GFP or AAV CAG-GFP-2A-Syt2 constructs were co-transfected with pHelper and pRC-DJ into HEK293 cells (ATCC). 72 hr later, cells were collected, lysed and loaded onto iodixanol gradient for centrifugation at 80,000g for 2 hr. The fraction with 40% iodixanol of the gradient was collected, washed and concentrated with 100,000 MWCO tube filter. The genomic titer of virus was measured by qPCR.

Stereotaxic injection: AAV CAG-Cre-GFP and AAV CAG-GFP-2A-Syt2 viruses were home-made. AAV retro-flippase, AAV Syn-Frt-Cre-IRES-tdTomato and rabies viruses were produced by the Janelia Farm Virus Core. AAV-retro-BFP-Cre was produced by Addgene. All the other AAVs were produced by the Stanford Virus Core. They were all in AAV-DJ serotype unless noted otherwise. The concentrations of virus used for stereotaxic injection were adjusted to 1.0×10^{12} genomic units/ml. Mice 45-60 days old (21 days for electrophysiological recording experiments) were anesthetized with tribromoethanol (300 mg/kg) and head-fixed with a stereotaxic device (KOPF model 1900). Viruses were injected using a glass micropipette attached to a 10 µl Hamilton syringe. The pipette tips were beveled to be sharp and smooth. AAVs were injected at a flow rate of 0.15 µl/min bilaterally for behavior experiments and on the left site for tracing experiments, unless otherwise noted. We waited for 2 min before and 4 min after each injection. AAVs were allowed to express for 3 weeks, after which mice were acutely sectioned for slice electrophysiology, histologically processed for anatomical tracing, or tested on the force plate and then histologically processed to confirm viral injection sites. For the rabies tracing experiments, 0.2 µl of a 1:1 volume mixture of AAV5-CAG-DIO-avian tumor virus receptor A (TVA)-mCherry and AAV8-CAG-DIO-glycoprotein (G) was injected into the left GRN of 6–8-weeks old PV^{cre}-$Syt2^{fl}$ or control mice (36). Two weeks later, 0.3 µl glycoprotein-deleted rabies virus was injected into the same brain region. One week later, mice were perfused and processed for imaging. The coordinates for small brain structures in millimeters were (anterior to Bregma, lateral to midline, ventral to dura; volume): CBN (–6.2, 1.75, 2.5; 0.2 µl). VAL/VM (–1.55, 1.1, 4; 0.2 µl). Red nucleus (–3.38, 0.75, 4.3; 0.2 µl). GRN (–6.8, 0.4, 5.15 → 4.25; 0.5 µl). Fastigial nucleus (–6.55, 1, 2.5; 0.05 µl). Interposed nucleus (–6.2, 1.75, 2.5; 0.05 µl). Dentate nucleus (–6, 2.2, 2.5; 0.05 µl). For each large brain area, viruses were injected at

multiple sites at 0.25 µl/min. The pipette tip was moved from the ventral coordinate to the dorsal coordinate during infusion at a steady speed in order to increase infection areas. Coordinates were: mPFC (1.25, 0.3, 1.4 → 0.4; 1 µl). Motor cortex (1.8, ±1.25, 0.9 → 0.1; 1 µl), (1.2, ±1.2, 0.9 → 0.1; 1 µl), (0.6, ±1.1, 0.9 → 0.1; 1 µl) and (–0.2, ±0.9, 0.9 → 0.1; 0.75 µl). Basal ganglia (0.4, ±2, 3.6 → 2; 2 µl), (–0.2, ±2.2, 3.6 → 2; 2 µl) and (–0.8, ±2.5, 3.6 → 2; 1 µl). Thalamus (–0.8, ±0.75, 4 → 3; 1 µl), (–1.31, ±1, 4.3 → 3.3; 2 µl) and (–1.9, ±1, 4 → 3; 2 µl). Cerebellum (–5.8, ±0.75, 2.3 → 0.7; 1.5 µl), (–5.8, ±2.25, 2.3 → 0.7; 1.5 µl), (–6.35, 0, 2.3 → 0.7; 1.5 µl), (–6.35, ±1.5, 2.3 → 0.7; 1.5 µl), (–6.35, ±3, 2.3 → 0.7, 1.5 µl), (–7, ±0.75, 2.1 → 0.7; 1.2 µl) and (–7, ±2.25, 2.1 → 0.7; 1.2 µl). Lateral cerebellar cortex (–5.8, ±2.75, 1; 1 µl), (–6.35, ±3, 1; 1 µl) and (–7, ±2.5, 1; 1 µl). Medial cerebellar cortex (–5.8, ±0.5, 1; 1 µl), (–6.35, ±0.5, 1; 1 µl) and (–7, ±0.5, 1; 1 µl).

Behavior: Both male and female mice 65-80 days old were used for all behavior tests unless noted otherwise. The mice genetic background and type of virus injected were coded and blinded to the experimenters.

Force plate: The design and applications of the same force plate actometer device were described in details in a previous study (22). We took advantage of this device's high sampling rate (100 Hz) of weight measurement and used a custom MATLAB script for data analysis. Mice were individually placed on the 28 × 28 cm plate and allowed to freely explore for 5 min unless noted otherwise. The raw data were divided into 3 sec segments and Fast Fourier Transformation was performed for each 3 sec segment. The power spectra were then averaged (Figure 1C). A "tremor index" was calculated by integrating the power value in the 9-12 Hz window. Power value in the 3-6 Hz window was used as the baseline. Real-time locomotion distance information could be derived from the same force plate raw data using the Pascal programs that came with

the force plate device. For ethanol injection experiments, animals were first measured on the force plate for 5 min, then given s.c. injections of 2.5 g/kg ethanol or saline and measured on the force plate for another 60 min. For harmaline injection experiments, 1mg/ml harmaline solution was prepared fresh by dissolving harmaline hydrochloride (Sigma, H1392) in saline. Animals were first measured on the force plate for 5 min, then given i.p. injections of 20 mg/kg harmaline and measured on the force plate for another 20 min. The action tremor was induced ~5 min after harmaline injection. The 5-10 min window was analyzed for harmaline-induced tremor.

Video analysis of tremor: To simultaneous collect video and force plate data, mice were placed on the force plate and surrounded by a small (13.35 × 8.40 × 20 cm) custom floorless acrylic chamber (TAP Plastic, Mountain View, CA) suspended over the force plate. Video recording was performed with an iPhone X mounted on top of the acrylic chamber using slow-motion mode (240 frames per second). Each behavioral session consisted of 2 min of free exploration, and the raw force plate data and video were saved for offline analysis. Using a tracking software Viewer III (BIOBSERVE), we extracted the XY-position of the animal's nose over time (Supplementary Figure 2, A and B). With a custom MATLAB script, these coordinates were bandpass filtered (9-12 Hz) to produce the filtered X and filtered Y signals. The envelopes (instantaneous amplitude) of these two signals were then calculated using the Hilbert transform (Supplementary Figure 2C and Supplementary Movie 1 and 2). Instantaneous tremor amplitude was calculated by taking the Euclidean norm of individual X and Y instantaneous amplitude. This was then averaged to calculate the average tremor amplitude for the session.

Spontaneous alternation Y maze: A light grey plastic Y maze was used to evaluate spatial working memory. The maze consisted of three arms separated by 120 degrees (dimensions of each arm: 40 × 10 × 17 cm). Mice around 4 weeks old were individually placed in the distal end

of one arm and allowed to freely explore the whole maze for 10 min. Completed arm entry was defined as the entering of a whole mouse including its tail into an arm. The sequences and total numbers of arm entries were recorded and analyzed with Viewer III tracking system. Visiting all three different arms consecutively was termed a 'correct' trial, and visiting one arm twice or more in three consecutive entries was termed wrong trial. We calculated the correct alternation percentage as (number of correct trials/total number of correct and wrong trials) × 100.

Novel object recognition: The same boxes used for open field test were used. On day 1, mice around 1 month old were given 10 min of habituation time individually in an empty box. On day 2, mice were individually placed in the box for 10 min with two identical objects, either T75 cell culture flask filled with bedding material or blocks of Legos. On day 3, one object was replaced with a novel object. Object location in chamber was randomized. Exploration behavior was recorded and analyzed with Viewer III tracking system. Recognition index was defined as the time spent on the novel object (or the left object for training phase) divided by the time spent on both objects.

Rotarod: An accelerating rotarod designed for mice (IITC Life Science) was used. The test consisted of three trials per day over the course of 3 days. The rotarod was activated after placing mice on the motionless rod. The rod accelerated from 4 to 40 revolutions per min in 5 min. Each trial ended when a mouse fell off, made one complete revolution while hanging on, or reached 300 sec.

Fear conditioning: On training day, mice were individually placed in fear conditioning chamber (Coulbourn Instruments) located in the center of a sound attenuating cubicle. The conditioning chamber was cleaned with 10% ethanol to provide a background odor. A ventilation fan provided a background noise at ~55 dB. After a 2 min exploration period, 3 tone-foot shock

pairings separated by 1 min intervals were delivered. The 85 dB 2 kHz tone lasted for 30 sec and the foot shock was 0.75 mA and lasted for 2 sec. The foot shocks co-terminated with the tone. The mice remained in training chamber for another 60 sec before being returned to home cages. In context test, mice were placed back into the original conditioning chamber for 5 min. The behavior of the mice was recorded with the Freezeframe software and analyzed with Freezeview software (Coulbourn Instruments). The running speed of mice were analyzed offline with Viewer III software. The average running speed of mice in the 2 min exploration period and 1 min period after each foot shock were summarized as an indication of contextual fear memory acquisition. The average running speed of mice in the 5 min period during context recall test was summarized as an indication of contextual fear memory retrieval.

Acute brain slice electrophysiology: P21 mice were used for viral injections and slice recordings were performed 20-30 days later. To increase visibility and obtain better recording quality of GRN neurons from adult brainstem slices, we slightly modified an N-Methyl-D-glucamine (NMDG)-based protocol (51). Specifically, 160 μm coronal brainstem slices were cut with a vibratome (VT1200S, Leica) in chilled cutting solution (in mM): 92 NMDG, 2.5 KCl, 1.25 NaH_2PO_4, 20 HEPES, 10 $MgSO_4$, 0.5 $CaCl_2$, 30 $NaHCO_3$, 25 D-glucose, 2 Thiourea, 5 Na-ascorbate, 3 Na-pyruvate (pH 7.3, adjusted with HCl) saturated with 95% O_2/5% CO_2 and recovered in the same NMDG-based cutting solution at 33 ^oC for 10-15 min. Slices were then transferred to room temperature oxygenated artificial cerebrospinal fluid (ACSF) containing (in mM): 119 NaCl, 2.5 KCl, 1.25 NaH_2PO_4, 2 $MgSO_4$, 2 $CaCl_2$, 26 $NaHCO_3$, 12.5 D-glucose, 2 Thiourea, 5 Na-ascorbate, 3 Na-pyruvate. After slices were transferred to a recording chamber, oxygenated ACSF was continuously perfused. Whole-cell voltage-clamp recordings were made with 3-4 MΩ pipettes filled with internal solution containing (in mM): 140 $CsMeSO_4$, 2 CsCl, 10

HEPES, 10 EGTA, 0.3 Na_2-GTP, 2 Mg-ATP, 7 Phosphocreatine, 5 TEA-Cl, 1 QX314 (pH 7.3, adjusted with CsOH). The whole-cell current signals were recorded with MultiClamp 700B and Clampex 10.4 data acquisition software (Molecular Device, LLC). Recordings were made from neurons in the GRN under bright field visualization with an upright microscope (BX51WI, Olympus). After establishment of the whole-cell configuration and equilibration of the intracellular pipette solution with the cytoplasm, sEPSCs were recorded by holding the cell at −70 mV. Spontaneous EPSCs were recorded for 5 minutes. A 473 nm laser (OEM Laser Systems) was used for light evoked EPSC recordings. Light was delivered through an optic fiber (200 μm, 0.22 NA) pointing towards the recorded area. Laser intensity was adjusted to get a maximal response without over stimulation. 50 Hz, 1 ms blue light was applied three repetitions at 20 sec intervals. Synaptic currents were analyzed offline using Clampfit 9 (Molecular Devices) software. Spontaneous events were analyzed using the template matching search and a minimum threshold of 5 pA and each event was visually inspected by an experimenter blind to the experiment conditions. Slice recording for mPFC neurons were performed similarly, except that a regular sucrose-based slice cutting protocol was used (35). sIPSCs were recorded by using a regular high chloride internal solution (36), including 20 μM 6-cyano-7-nitroquinoxaline-2,3-dione (CNQX), 50 μM (2R)-amino-5-phosphonovaleric acid (APV) in the ACSF, and clamping the neurons at −70 mV. Evoked IPSCs were recorded by using the same internal solution as GRN recordings, including 20 μM CNQX, 50 μM APV in the ACSF, and clamping the neurons at 0 mV.

Histology: Mice were deep anesthetized with tribromoethanol and perfused with 10 ml of PBS followed by 10 ml of fixative (4% paraformaldehyde diluted in PBS). The brains were removed and post-fixed in 4^{o}C overnight and then immersed in 30% sucrose solution for two days before

being sectioned at 50 μm thicknesses on a cryostat (Leica CM3050 S). The free-floating brain sections were collected in PBS. For injection site verification, the sections were directly mounted onto glass slides with Vectashield mounting medium with DAPI, except for results shown in Supplementary Figure 7D, in which mounting medium without DAPI was used. For tracing experiments, one out of every five sections were collected for the whole brain. For immunohistochemistry, standard procedures were followed (36). We used primary antibodies to Syt2 (rabbit, A320, 1:1000, ref 19), Vglut1 (guinea pig, Millipore AB5905, 1:1000) and Vglut2 (guinea pig, Millipore AB2251, 1:1000). A scanning microscope (BX61VS, Olympus) was used to scan fluorescent images for whole brain slices and a confocal microscope (Nikon A1) was used for higher resolution imaging.

Statistics: All results are presented as mean ± SEM and were analyzed by the OriginPro 8 software (OriginLab Corp.). No statistical methods were used to pre-determine sample sizes but our sample sizes are similar to those reported in previous publications. Normality tests and F tests for equality of variance were performed before choosing the statistical test. Unless otherwise indicated, statistics were based on two-sided unpaired or paired t-tests or Mann-Whitney tests (for datasets that were not normally distributed) for two-group comparisons. $P < 0.05$ was considered significant ($*P < 0.05$, $**P < 0.01$, $***P < 0.001$). Results in Figure 1I were analyzed with one-way repeated measures ANOVA with post hoc analysis (Tukey's). Whenever possible, experiment conditionings were blinded to experimenters. Injection sites and viral expression were confirmed for all animals. Mice showing incorrect injection sites were excluded from data analysis.

Study approval: All animal experiments were conducted following protocols approved by Administrative Panel on Laboratory Animal Care at Stanford University.

Author contributions: M.Z., W.X. and T.C.S. designed the experiments. M.Z., M.D.M. and W.X. performed the experiments. M.Z. and T.C.S. analyzed the data and wrote the manuscript with input from all authors.

Acknowledgments: We thank V. Cheepurupalli, J. Vu and M. Tran for technical assistance; D. Anderson for providing Prkcd^{cre} mice; H. Wu and C. Halpern for advices on clinical aspects of the project. The work was supported by a National Institute of Health (NIH)/National Institute of Mental Health grant (no. MH052804 to T.C.S.) and a NIH/National Institute of Neurological Disorders and Stroke grant (no. 1K01NS105155 to M.Z.).

References:

1. Louis ED, and Ferreira JJ. How common is the most common adult movement disorder? Update on the worldwide prevalence of essential tremor. *Mov. Disord*. 2010;25(5):534-41.
2. Haubenberger D, and Hallett M. Essential Tremor. *N. Eng. J. Med*. 2018;378(19):1802-10.
3. Dogu O, et al. Prevalence of essential tremor: door-to-door neurologic exams in Mersin Province, Turkey. *Neurology*. 2003;61(12):1804-6.
4. Moghal S, Rajput AH, D'Arcy C, and Rajput R. Prevalence of movement disorders in elderly community residents. *Neuroepidemiology*. 1994;13(4):175-8.
5. Louis ED. Understanding essential tremor: progress on the biological front. *Curr. Neuro. Neurosci. Rep*. 2014;14(6):450.
6. Llinas R, and Volkind RA. The olivo-cerebellar system: functional properties as revealed by harmaline-induced tremor. *Exp. Brain Res*. 1973;18(1):69-87.
7. Deuschl G, and Elble RJ. The pathophysiology of essential tremor. *Neurology*. 2000;54(11 Suppl 4):S14-20.
8. Handforth A. Harmaline tremor: underlying mechanisms in a potential animal model of essential tremor. *Tremor Other Hyperkinet Mov (N Y)*. 2012;2.
9. Louis ED, et al. Neuropathological changes in essential tremor: 33 cases compared with 21 controls. *Brain*. 2007;130(Pt 12):3297-307.
10. Louis ED, and Vonsattel JP. The emerging neuropathology of essential tremor. *Mov. Disord*. 2008;23(2):174-82.

11. Yu M, et al. Increased number of Purkinje cell dendritic swellings in essential tremor. *Eur. J. Neurol*. 2012;19(4):625-30.

12. Sharifi S, Nederveen AJ, Booij J, and van Rootselaar AF. Neuroimaging essentials in essential tremor: a systematic review. *NeuroImage Clin*. 2014;5:217-31.

13. Benito-Leon J, and Labiano-Fontcuberta A. Linking Essential Tremor to the Cerebellum: Clinical Evidence. *Cerebellum*. 2016;15(3):253-62.

14. Miwa H. Rodent models of tremor. *Cerebellum*. 2007;6(1):66-72.

15. Pan MK, Ni CL, Wu YC, Li YS, and Kuo SH. Animal Models of Tremor: Relevance to Human Tremor Disorders. *Tremor Other Hyperkinet Mov (N Y)*. 2018;8:587.

16. Kuo SH, et al. Current Opinions and Consensus for Studying Tremor in Animal Models. *Cerebellum*. 2019.

17. Kralic JE, et al. Genetic essential tremor in gamma-aminobutyric acidA receptor alpha1 subunit knockout mice. *J. Clin. Investig*. 2005;115(3):774-9.

18. White JJ, et al. Pathogenesis of severe ataxia and tremor without the typical signs of neurodegeneration. *Neurobiol. Dis*. 2016;86:86-98.

19. Pang ZP, et al. Synaptotagmin-2 is essential for survival and contributes to Ca2+ triggering of neurotransmitter release in central and neuromuscular synapses. *J. Neurosci*. 2006;26(52):13493-504.

20. Sun J, Pang ZP, Qin D, Fahim AT, Adachi R, and Sudhof TC. A dual-Ca2+-sensor model for neurotransmitter release in a central synapse. *Nature*. 2007;450(7170):676-82.

21. Luo F, and Sudhof TC. Synaptotagmin-7-Mediated Asynchronous Release Boosts High-Fidelity Synchronous Transmission at a Central Synapse. *Neuron*. 2017;94(4):826-39 e3.

22. Fowler SC, et al. A force-plate actometer for quantitating rodent behaviors: illustrative data on locomotion, rotation, spatial patterning, stereotypies, and tremor. *J. Neurosci. Methods*. 2001;107(1-2):107-24.

23. Boecker H, et al. The effect of ethanol on alcohol-responsive essential tremor: a positron emission tomography study. *Ann. Neurol*. 1996;39(5):650-8.

24. Sommeijer JP, and Levelt CN. Synaptotagmin-2 is a reliable marker for parvalbumin positive inhibitory boutons in the mouse visual cortex. *PLOS ONE*. 2012;7(4):e35323.

25. Sudhof TC. Synaptotagmins: why so many? *J. Biol. Chem*. 2002;277(10):7629-32.

26. Benabid AL, et al. Long-term suppression of tremor by chronic stimulation of the ventral intermediate thalamic nucleus. *Lancet*. 1991;337(8738):403-6.

27. Flora ED, Perera CL, Cameron AL, and Maddern GJ. Deep brain stimulation for essential tremor: a systematic review. *Mov. Disord*. 2010;25(11):1550-9.

28. Deuschl G, Raethjen J, Hellriegel H, and Elble R. Treatment of patients with essential tremor. *Lancet*. 2011;10(2):148-61.

29. Lein ES, et al. Genome-wide atlas of gene expression in the adult mouse brain. *Nature*. 2007;445(7124):168-76.

30. Haubensak W, et al. Genetic dissection of an amygdala microcircuit that gates conditioned fear. *Nature*. 2010;468(7321):270-6.

31. Chen S, and Hillman DE. Compartmentation of the cerebellar cortex by protein kinase C delta. *Neuroscience*. 1993;56(1):177-88.

32. Hu H, Gan J, and Jonas P. Interneurons. Fast-spiking, parvalbumin(+) GABAergic interneurons: from cellular design to microcircuit function. *Science*. 2014;345(6196):1255263.

33. Esposito MS, Capelli P, and Arber S. Brainstem nucleus MdV mediates skilled forelimb motor tasks. *Nature*. 2014;508(7496):351-6.

34. Ferreira-Pinto MJ, Ruder L, Capelli P, and Arber S. Connecting Circuits for Supraspinal Control of Locomotion. *Neuron*. 2018;100(2):361-74.

35. Xu W, and Sudhof TC. A neural circuit for memory specificity and generalization. *Science*. 2013;339(6125):1290-5.

36. Zhou M, Liu Z, Melin MD, Ng YH, Xu W, and Sudhof TC. A central amygdala to zona incerta projection is required for acquisition and remote recall of conditioned fear memory. *Nat. Neurosci*. 2018;21(11):1515-9.

37. Xu W, Morishita W, Buckmaster PS, Pang ZP, Malenka RC, and Sudhof TC. Distinct neuronal coding schemes in memory revealed by selective erasure of fast synchronous synaptic transmission. *Neuron*. 2012;73(5):990-1001.

38. Willner P. The validity of animal models of depression. *Psychopharmacology*. 1984;83(1):1-16.

39. Elble RJ, Schieber MH, and Thach WT, Jr. Activity of muscle spindles, motor cortex and cerebellar nuclei during action tremor. *Brain Res*. 1984;323(2):330-4.

40. Monzee J, Drew T, and Smith AM. Effects of muscimol inactivation of the cerebellar nuclei on precision grip. *J. Neurophy*. 2004;91(3):1240-9.

41. Paris-Robidas S, et al. Defective dentate nucleus GABA receptors in essential tremor. *Brain*. 2012;135(Pt 1):105-16.

42. Brooks VB, Kozlovskaya IB, Atkin A, Horvath FE, and Uno M. Effects of cooling dentate nucleus on tracking-task performance in monkeys. *J. Neurophy*. 1973;36(6):974-95.

43. Cooke JD, and Thomas JS. Forearm oscillation during cooling of the dentate nucleus in the monkey. *Can. J. Physiol. Pharmacol*. 1976;54(4):430-6.

44. Xu J, Pang ZP, Shin OH, and Sudhof TC. Synaptotagmin-1 functions as a Ca2+ sensor for spontaneous release. *Nat. Neurosci*. 2009;12(6):759-66.

45. Sudhof TC. A molecular machine for neurotransmitter release: synaptotagmin and beyond. *Nat. Med*. 2013;19(10):1227-31.

46. Wolpert DM, Ghahramani Z, and Jordan MI. An internal model for sensorimotor integration. *Science*. 1995;269(5232):1880-2.

47. Boyden ES, Katoh A, and Raymond JL. Cerebellum-dependent learning: the role of multiple plasticity mechanisms. Annu. Rev. Neurosci. 2004;27:581-609.

48. Chen C, Arai I, Satterfield R, Young SM, Jr., and Jonas P. Synaptotagmin 2 Is the Fast Ca(2+) Sensor at a Central Inhibitory Synapse. *Cell Rep*. 2017;18(3):723-36.

49. Testa CM. Key issues in essential tremor genetics research: Where are we now and how can we move forward? *Tremor Other Hyperkinet Mov (N Y)*. 2013;3.

50. Tio M, and Tan EK. Genetics of essential tremor. *Parkinsonism Relat. Disord*. 2016;22 Suppl 1:S176-8.

51. Zhao S, et al. Cell type-specific channelrhodopsin-2 transgenic mice for optogenetic dissection of neural circuitry function. *Nat. Methods*. 2011;8(9):745-52.

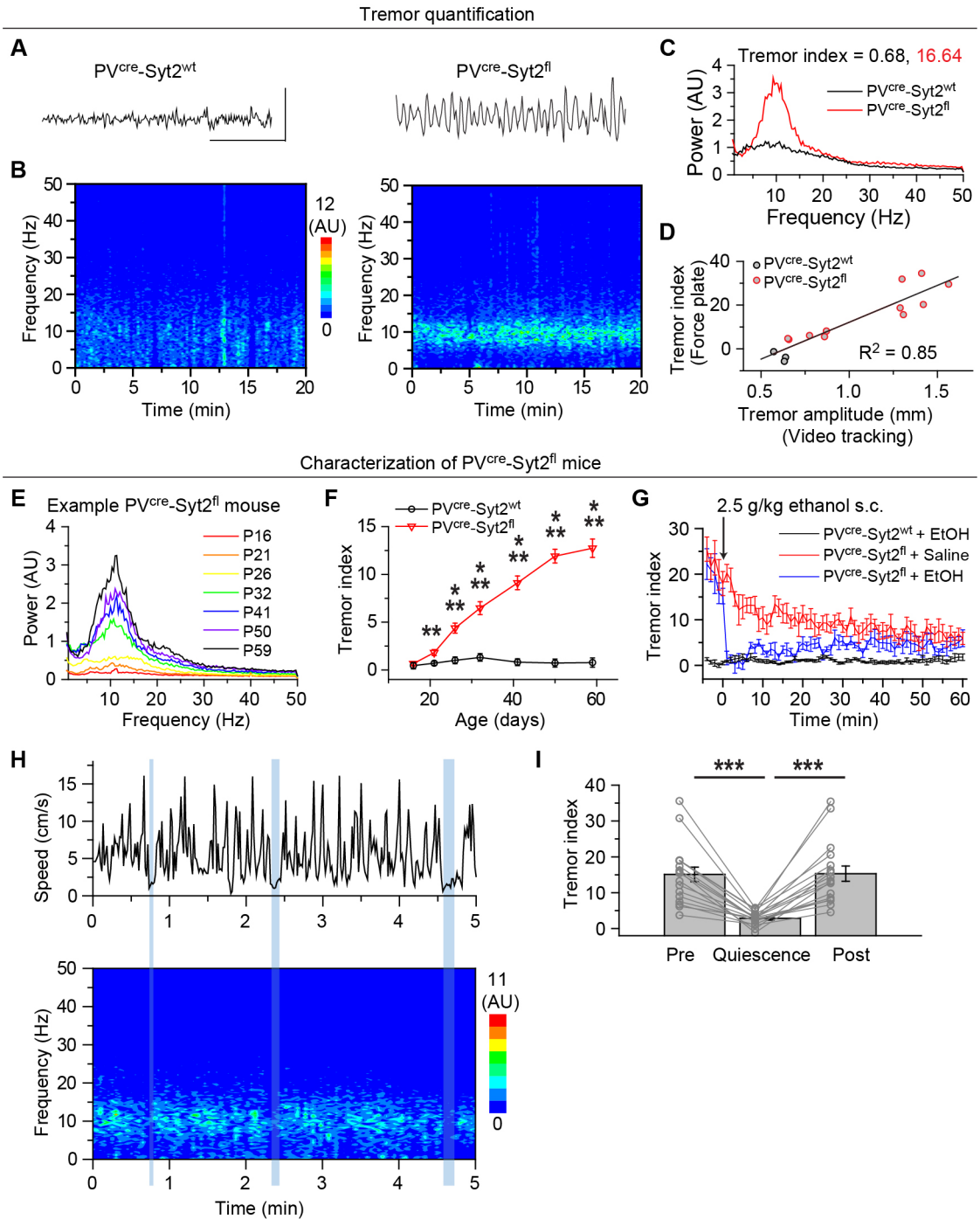

Figure 1. **PV^{cre}-Syt2^{fl} mice: an animal model for action tremor**.

(**A-C**) Exemplary tremor recordings on a force plate to illustrate the tremor observed in PV^{cre}-Syt2^{fl} mice compared to PV^{cre}-Syt2^{wt} mice. (**A**), raw data of 3 sec weight measurement using the

force-plate actometer; (**B**), spectrograph calculated from 20 min force-plate measurements; (**C**), averaged power spectrum from data in **B**. The tremor index was calculated by integrating the power in the 9-12 Hz range and using the averaged power in the 3-6 Hz range as baseline. (**D**) Correlation of the tremor index measured on a force plate and the tremor amplitude monitored simultaneously by video tracking in PV^{cre}-$Syt2^{fl}$ and control mice at different ages. (**E**) Power spectra of force plate measurements from a representative PV^{cre}-$Syt2^{fl}$ mouse at different ages. (**F**) Summary plot of the tremor index of PV^{cre}-$Syt2^{wt}$ and PV^{cre}-$Syt2^{fl}$ mice as a function of age (n = 19 PV^{cre}-$Syt2^{wt}$, n = 18 PV^{cre}-$Syt2^{fl}$). (**G**) Summary plot of the tremor index of PV^{cre}-$Syt2^{fl}$ and control mice as a function of time after an s.c. injection of ethanol, with PV^{cre}-$Syt2^{fl}$ mice injected with saline used as a further control (n = 5 control+EtOH, n = 7 PV^{cre}-$Syt2^{fl}$+Saline, n = 6 PV^{cre}-$Syt2^{fl}$+EtOH). (**H**) Exemplary simultaneous measurements of the movements and tremor in a PV^{cre}-$Syt2^{fl}$ mouse. Episodes longer than 3 sec with speed smaller than 2.5 cm/s are indicated by vertical blue shaded bars. (**I**) Summary graph of the tremor index of PV^{cre}-$Syt2^{fl}$ mice before, during and after periods of quiescence lasting longer than 3 sec (n = 17). For **F**, **G** and **I**, data are shown as means ± SEM from at least 3 independent litters. $^{**}P < 0.01$, $^{***}P < 0.001$, two-sided unpaired t test (**F**); $^{***}P < 0.001$, one-way ANOVA (**I**). Scale bars: 20 g (**A**, vertical); 1 s (**A**, horizontal);

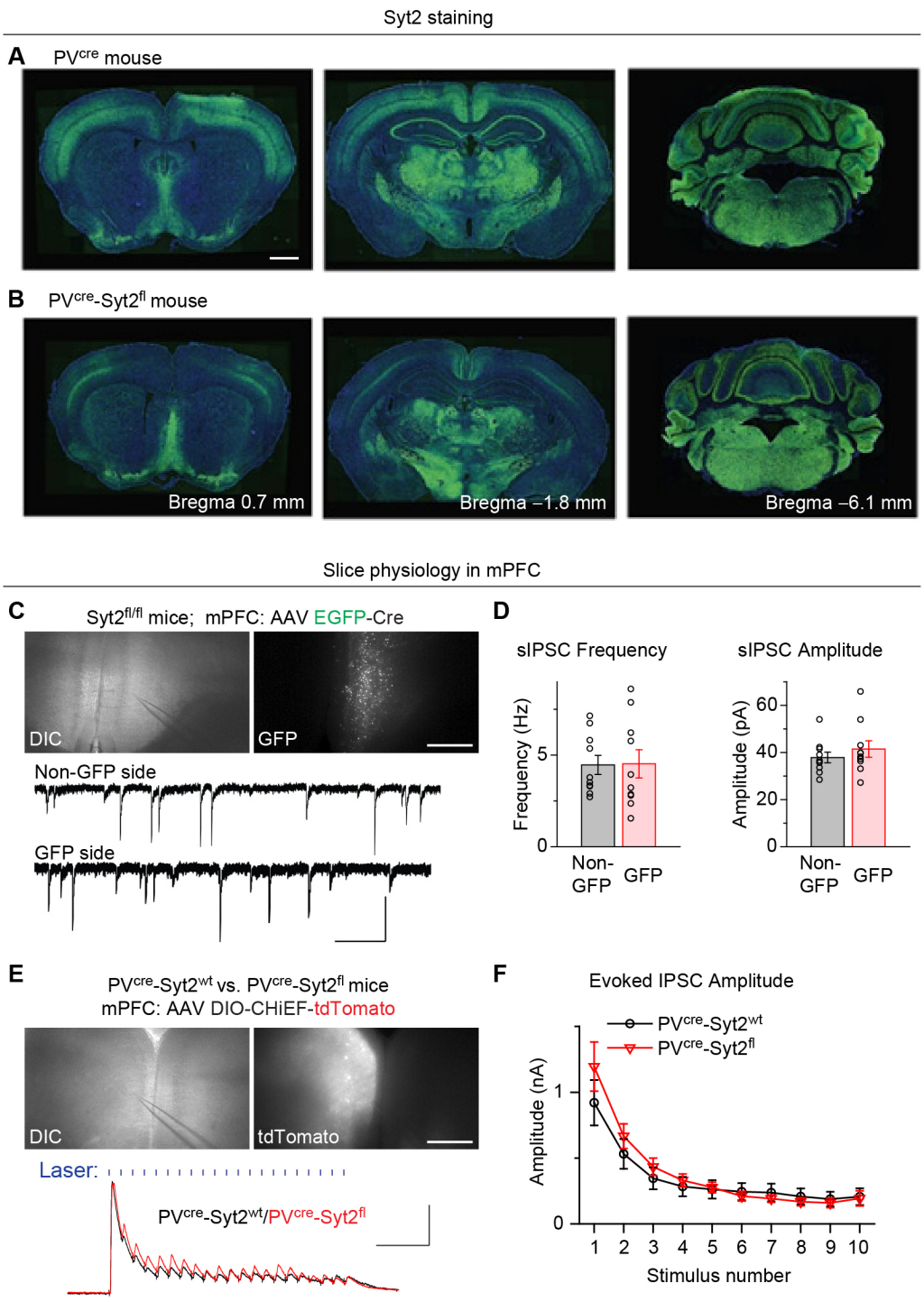

Figure 2. Syt2 is prominently expressed in cortical PV$^+$ neurons but deletion of Syt2 from mPFC PV$^+$ neurons does not impair their synaptic releases.

(**A** and **B**) Representative images of different coronal brain sections showing the immunostaining of Syt2 for PV^{cre} (**A**) and PV^{cre}-$Syt2^{fl}$ (**B**) mice. (**C** and **D**) Deleting Syt2 from mPFC PV^{+} neurons does not affect sIPSCs received by pyramidal neurons. (**C**) Top, DIC and fluorescence images showing the expressing of EGFP-Cre in the mPFC of a $Syt2^{fl/fl}$ mouse. Slice is arranged upright; Bottom, example traces showing the sIPSCs recorded from mPFC pyramidal neurons with (GFP side) and without (non-GFP side) deletion of Syt2 from PV^{+} neurons. (**D**) Summary graph of the sIPSC frequency (left) and amplitude (right) recorded from mPFC pyramidal neurons on GFP and non-GFP sides (n = 10 non-GFP, n = 10 GFP for both frequency and amplitude). (**E** and **F**) Deleting Syt2 from mPFC PV^{+} neurons does not affect evoked IPSCs received by pyramidal neurons. (**E**) Top, DIC and fluorescence images showing the expressing of Cre-dependent CHiEF-tdTomato in mPFC PV^{+} neurons of a PV^{cre}-$Syt2^{fl}$ mouse. Slice is arranged upright; Bottom, example traces showing the 1ms, 45 Hz blue laser (shown as blue vertical bars) evoked IPSCs recorded from mPFC pyramidal neurons in a PV^{cre}-$Syt2^{fl}$ mouse and a control mouse. (**F**) Summary graph of 45 Hz light evoked IPSC amplitude (in response to the first 10 train stimuli) recorded from mPFC pyramidal neurons in control and PV^{cre}-$Syt2^{fl}$ mice (n = 9 control, n = 7 PV^{cre}-$Syt2^{fl}$). For **D** and **F**, data are shown as means ± SEM from at least 3 independent litters. Scale bars: 1 mm (**A**); 0.5 mm (**C**, top); 50 pA (**C**, vertical); 0.5 S (**C**, bottom horizontal); 0.5 mm (**E**, top); 0.5 nA (**E**, vertical); 0.1 s (**E**, bottom horizontal).

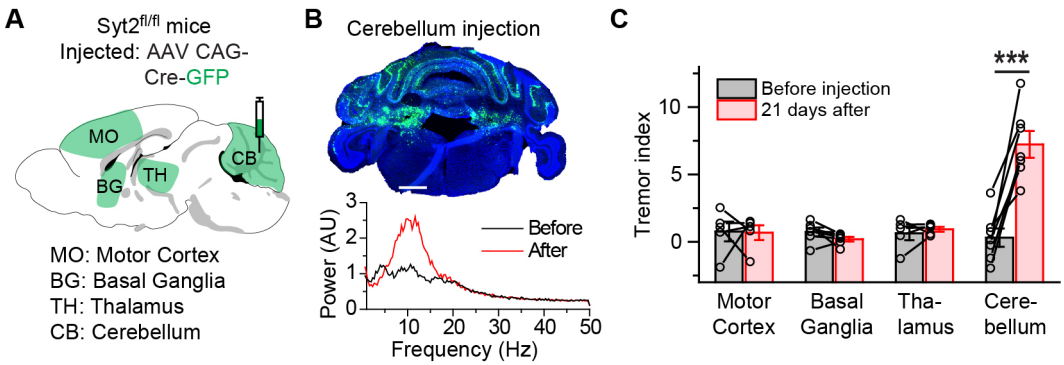

Figure 3. **Syt2 deletion from the cerebellum is sufficient to generate an action tremor**.

(**A**) Stereotactic injection strategy of AAVs encoding Cre-GFP into one of four brain regions: the motor cortex, basal ganglia, thalamus or cerebellum. (**B**) Top, a representative image showing the expression of Cre-GFP in the cerebellum of Syt2$^{fl/fl}$ mice; Bottom, power spectrum of force plate measurements from the same mouse before and after viral injection. Also see Supplementary Video 5 and Supplementary Figure 5. (**C**) Summary graph of the tremor index before and after injections of AAV Cre-GFP into different brain regions (n = 5 MO, n = 6 BG, n = 5 TH, n = 7 CB). Please see methods for our approaches to infect these large brain areas. For **C**, data are shown as means ± SEM from at least 3 independent litters. ***$P < 0.001$, two-sided paired t test. Scale bar: 1 mm (**B**).

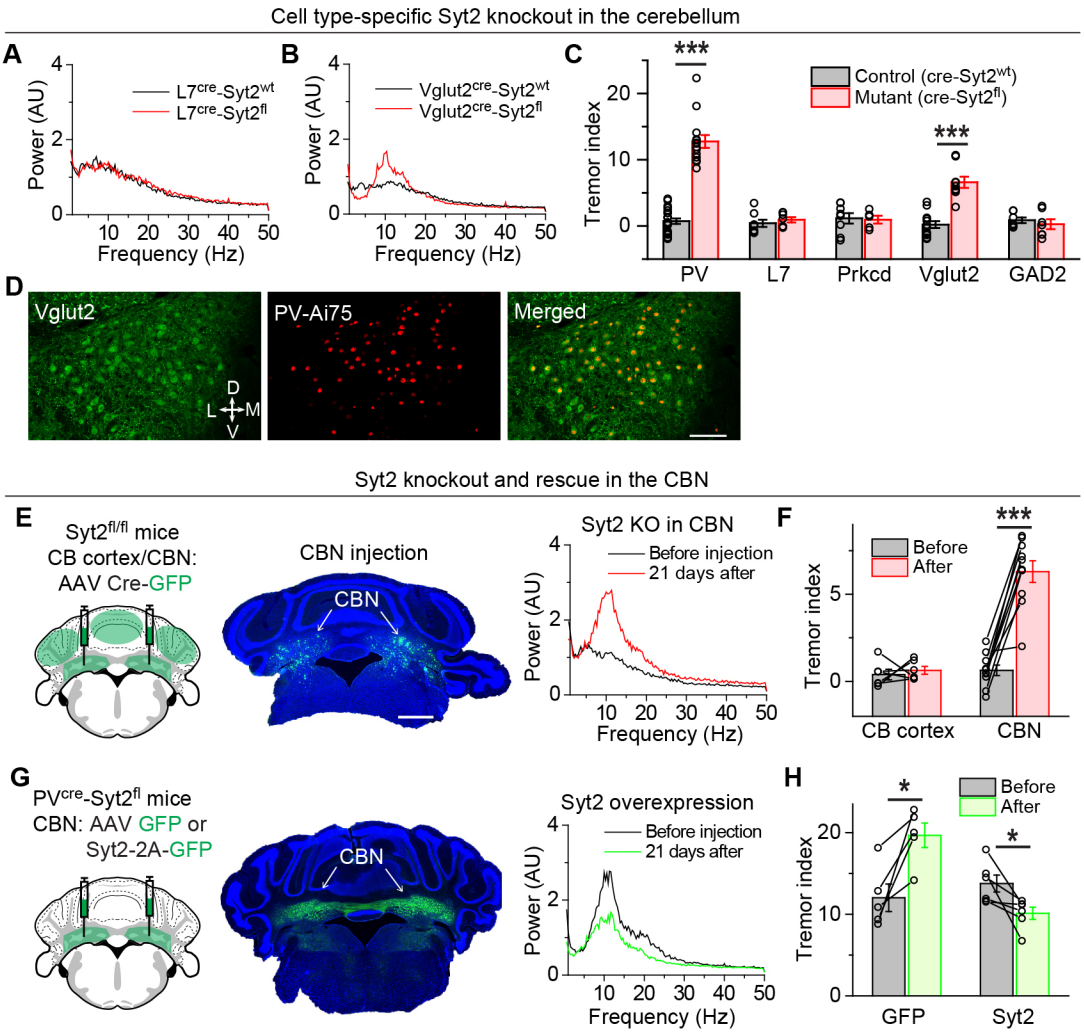

Figure 4. **Syt2 deletion from PV^{+} neurons in the CBN is sufficient to generate an action tremor**.

(**A** and **B**) Power spectra of force plate measurements from representative control and L7^{cre}-Syt2^{fl} mice (**A**) or control and Vglut2^{cre}-Syt2^{fl} mice (**B**). (**C**) Summary graph of the tremor index of Syt2$^{fl/fl}$ mice after crossing with the five different Cre mouse lines (n = 19 PV-control, n = 18 PV-mutant, n = 8 L7-control, n = 7 L7-mutant, n = 8 Prkcd-control, n = 5 Prkcd-mutant, n = 12 Vglut2-control, n = 9 Vglut2-mutant, n = 7 GAD2-control, n = 7 GAD2-mutant). (**D**) Representative images of the CBN section from a PV^{cre}-Ai75 mouse showing the co-localization of antibody-labelled Vglut2 neurons and genetically labelled PV^{+} neurons in CBN. (**E**) Left,

stereotactic injection strategy of AAVs encoding Cre-GFP into the CBN or the cerebellar cortex of $Syt2^{fl/fl}$ mice; Middle, a representative image showing the bilateral expression of Cre-GFP in the CBN; Right, power spectrum of force plate measurements from the same $Syt2^{fl/fl}$ mouse before and after Cre-GFP expression in the CBN. (**F**) Summary graph of tremor index before and after Cre-GFP expression in the CBN or cerebellar cortex of $Syt2^{fl/fl}$ mice (n =6 CB cortex, n = 10 CBN). (**G** and **H**) Figure panels arranged the same way as in **E** and **F**, except that AAVs encoding GFP or Syt2-2A-GFP were injected into the CBN of PV^{cre}-$Syt2^{fl}$ mice (n = 5 GFP, n = 6 Syt2). For **C**, **F** and **H**, data are shown as means ± SEM from at least 3 independent litters. ***$P < 0.001$, two-sided unpaired t test (**C**); ***$P < 0.001$, two-sided paired t test (**F**); *$P < 0.05$, two-sided paired t test (**H**). Scale bars: 100 μm (**D**); 1 mm (**E**);

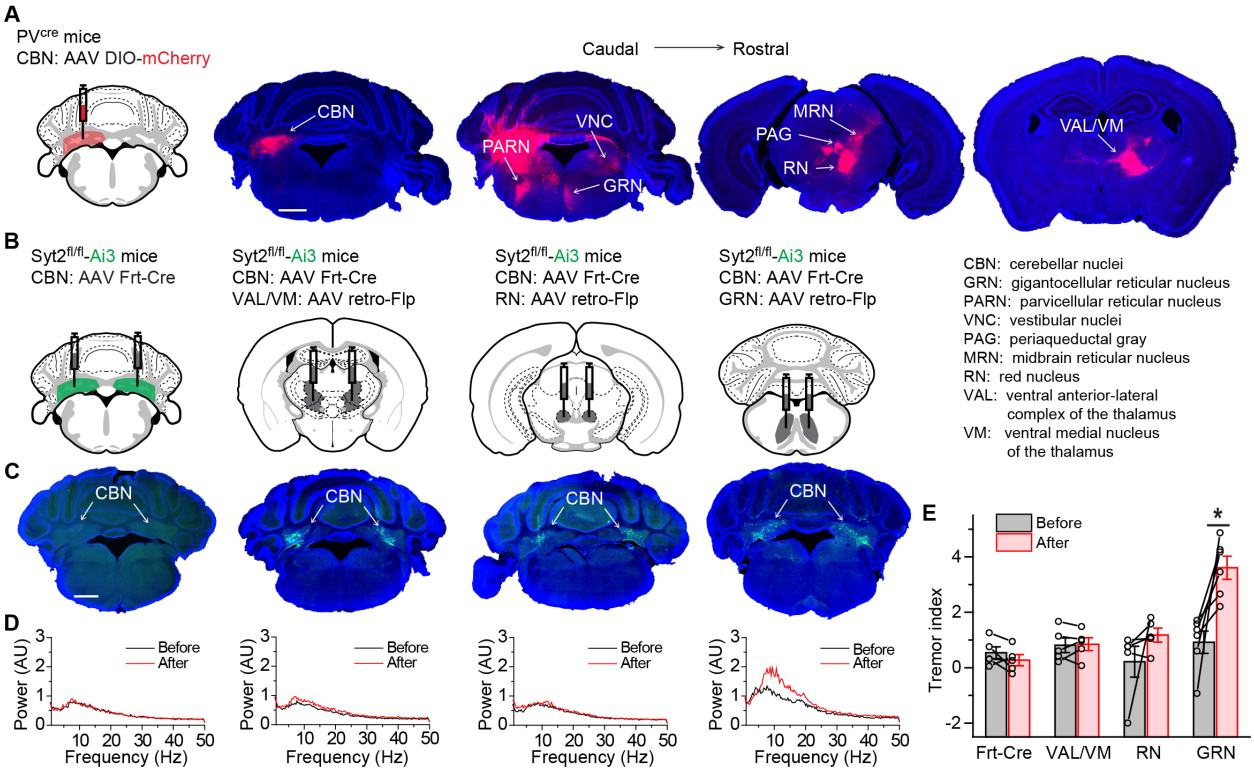

Figure 5. Identification of CBN downstream targets that induce the action tremor.

(**A**) Representative images of anterograde tracing experiments of projections from PV^{+} neurons in CBN to other brain regions (left, stereotactic injection strategy of AAVs encoding DIO-mCherry into the CBN of a PV^{cre} mice; right images, coronal slices arranged in a caudal → rostral direction showing mCherry expression in the indicated brain regions [note that the three fluorescent images on the right were overexposed to reveal the axon terminal signals]). (**B**) Stereotactic injection strategies of AAVs encoding flippase-dependent Cre (Frt-Cre) in the CBN (most left) or both Frt-Cre in the CBN and AAV retro-flippase in the VAL/VM, red nucleus or GRN of $Syt2^{fl/fl}$ crossed with EYFP reporter (Syt2-Ai3) mice (three on the right). (**C**) Representative images showing the expression of EYFP in CBN for each injection experiment depicted in **B**. (**D**) Power spectra of force plate measurements from representative Syt2-Ai3 mice before and after the corresponding injections shown in **B** and **C**. (**E**) Summary graph of the

tremor index before and after each injection shown in **B** (n = 5 Frt-Cre, n = 5 VAL/VM, n = 6 RN, n = 5 GRN). For **E**, data are shown as means ± SEM from at least 3 independent litters. *P < 0.05, Mann-Whitney test (**E**). Scale bars: 1 mm (**A**); 1 mm (**C**).

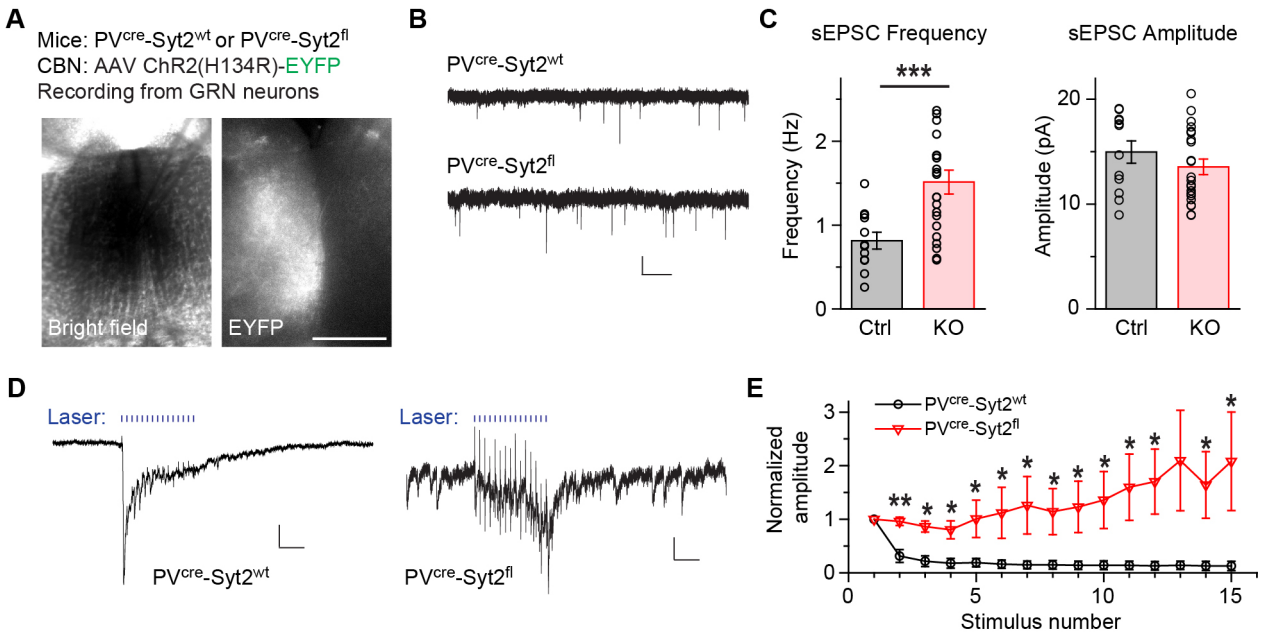

Figure 6. Loss of fast synchronous neurotransmitter release at CBN → GRN synapses may induce the action tremor.

(**A**) Bright field and fluorescence images of GRN sections from PV^{cre}-Syt2^{fl} or control mice showing ChR2-EYFP expression in nerve terminals originating from CBN neurons. Slice is arranged upright. (**B**) Example traces showing spontaneous EPSCs recorded from GRN neurons in slices from control and PV^{cre}-Syt2^{fl} mice. (**C**) Summary graph of the sEPSC frequency (left) and amplitude (right) recorded from GRN neurons in slices from control and PV^{cre}-Syt2^{fl} mice (n = 12 Ctrl, n = 22 PV^{cre}-Syt2^{fl} for both Frequency and Amplitude). (**D**) Example traces showing 1 ms, 50 Hz blue laser evoked EPSCs recorded from GRN neurons in control (left) and PV^{cre}-Syt2^{fl} (right) slices. (**E**) Summary of 50 Hz light evoked EPSC amplitude recorded from GRN neurons in control and PV^{cre}-Syt2^{fl} slices. All amplitudes are normalized to the first EPSC responses for both groups (n = 5 Control, n = 7 PV^{cre}-Syt2^{fl}). For **C** and **E**, data are shown as means ± SEM from at least 3 independent litters. ***P < 0.001, two-sided unpaired t test (**C**); *P < 0.05, **P < 0.01, two-sided unpaired t test (**E**). Scale bars: 0.5 mm (**A**); 10 pA (**B**, vertical); 1 s

(**B**, horizontal); 20 pA (**D** vertical left); 0.1 s (**D** horizontal left); 4 pA (**D** vertical right); 0.1 s (**D** horizontal right).

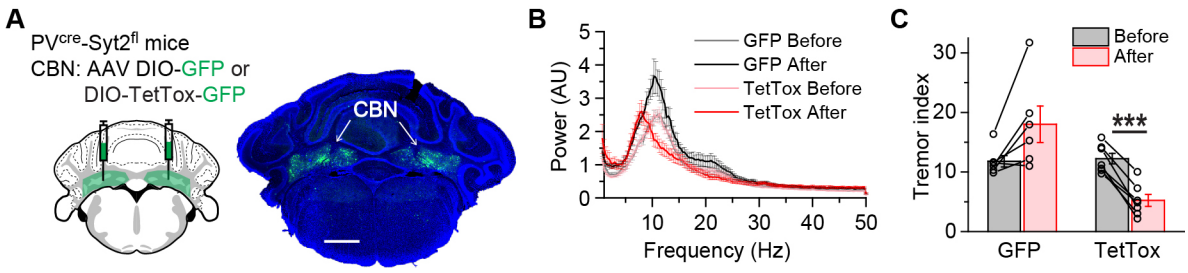

Figure 7. Blocking neurotransmitter release in CBN neurons rescues the action tremor of PV^{cre}-Syt2^{fl} mice.

(**A**) Left, stereotactic injection strategy of AAVs encoding DIO-GFP or DIO-TetTox-GFP into the CBN of PV^{cre}-Syt2^{fl} mice, resulting in expression of GFP only or tetanus toxin light chain fused to GFP only in PV^{+} neurons; Right, a representative image showing the bilateral expression of GFP in the CBN. (**B**) Averaged power spectrum of force plate measurements from PV^{cre}-Syt2^{fl} mice before and after injection of AAVs encoding GFP or TetTox-GFP (n = 6 GFP, n = 7 TetTox). Note that after TetTox expression, the tremor not only decreased, but the peak tremor frequency also shifted to ~8 Hz. (**C**) Summary graph of the tremor index before and after injection of AAVs encoding GFP or TetTox-GFP in the CBN of PV^{cre}-Syt2^{fl} mice (n = 6 GFP, n = 7 TetTox). For **B** and **C**, data are shown as means ± SEM from at least 2 independent litters. ***$P < 0.001$, two-sided paired t test (**C**). Scale bar: 1 mm (**A**).

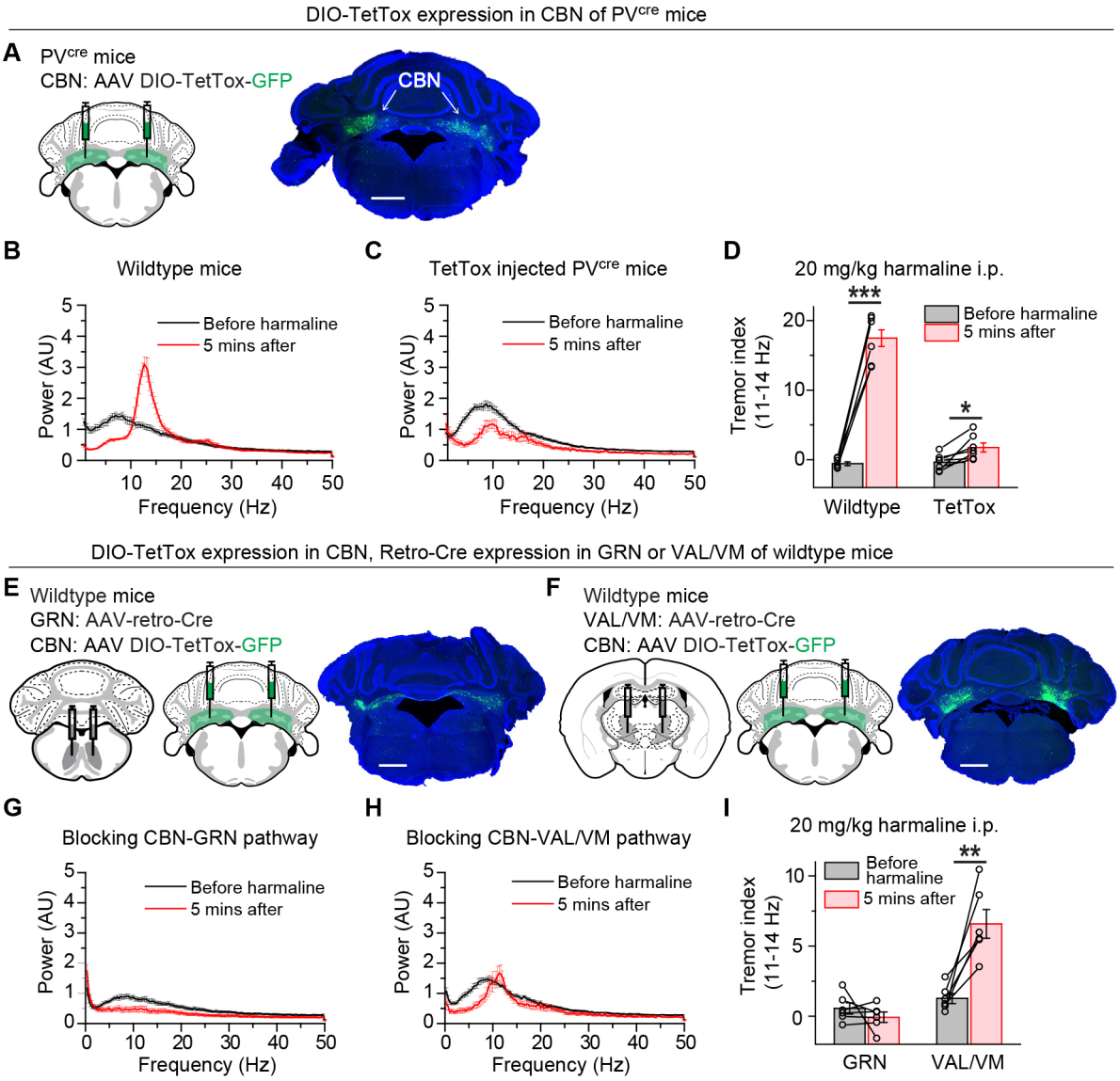

Figure 8. Blocking neurotransmitter release in CBN neurons rescues the action tremor of harmaline-injected mice.

(**A**) Left, stereotactic injection strategy of AAVs encoding DIO-TetTox-GFP into the CBN of PV^{cre} mice; Right, a representative image showing the bilateral expression of GFP in the CBN. (**B**) Averaged power spectrum of force plate measurements from wildtype mice before and 5 mins after harmaline injection (n = 7). (**C**) Averaged power spectrum of force plate measurements from TetTox-injected mice before and 5 mins after harmaline injection (n = 7).

(**D**) Summary of tremor index in the 11-14 Hz range (see methods) before and 5 mins after harmaline intraperitoneal (i.p.) injection in wildtype and TetTox-injected mice (n = 7 Wildtype, n = 7 TetTox). (**E**) Left and middle, stereotactic injection strategy of AAV-retro-Cre into the GRN and AAV DIO-TetTox-GFP into the CBN of wildtype mice; Right, a representative image showing the bilateral expression of GFP in the CBN. (**F**) The same as in **E**, except that the AAV-retro-Cre virus was injected into the VAL/VM. (**G**) Averaged power spectrum of force plate measurements from GRN-injected mice before and 5 mins after harmaline injection (n = 6). (**H**) Averaged power spectrum of force plate measurements from VAL/VM-injected mice before and 5 mins after harmaline injection (n = 6). (**I**) Summary of tremor index in the 11-14 Hz range before and 5 min after harmaline i.p. injection in GRN- and VAL/VM-injected mice (n = 6 GRN, n = 6 VAL/VM). For **B-D** and **G-I**, data are shown as means ± SEM from at least 2 independent litters. *$P < 0.05$, ***$P < 0.001$, two-sided paired t test (**D**); **$P < 0.01$, two-sided paired t test (**I**). Scale bar: 1 mm (**A**); 1 mm (**E**); 1 mm (**F**).

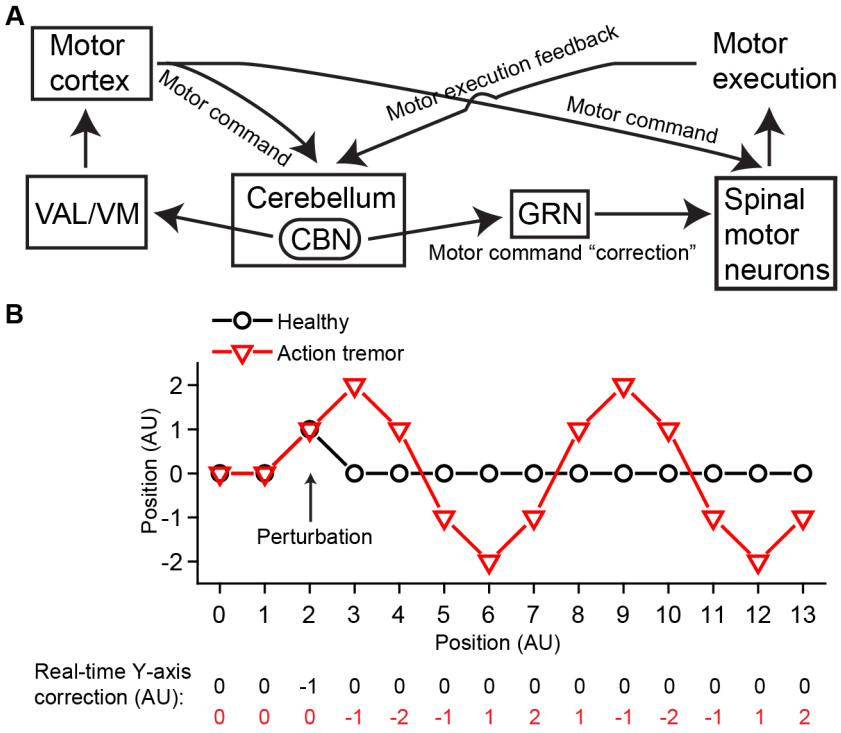

Figure 9. **Model for the generation of action tremor**

(**A**) Schematic diagram of the neural circuit controlling the real-time correction of movement command signals. (**B**) Simplified simulation showing how delayed online movement correction could generate oscillatory movement. Here the planned path is a straight line from (0, 0) to (13, 0). Assuming movement at (2, 0) is deviated to (2, 1) due to a perturbation. In healthy animals, the movement is compensated by the Y-axis "correction" signal "–1" in real-time and continues its planned trajectory. In action tremor animals, we posit the "correction" signal is delayed by a fixed time period (time needed to move between two ticks on the X-axis), as shown by the row of numbers in red at the bottom. The deviated movement at (2, 1) is not compensated and continues on the wrong trajectory to (3, 2) where it starts to be partially compensated by the delayed "correction" signal "–1". Continuing with this delayed Y-axis correction, the movement

exhibits an oscillatory pattern. In this simplified simulation, as the duration of the fixed temporal delay increases, tremor amplitude increases and frequency decreases.

Table 1. Characteristics of PV^{cre}-$Syt2^{fl}$ mouse model.

Chracteristic	ET patients	Harmaline mouse model	PV^{cre}-$Syt2^{fl}$ mouse model
Frequency **(Hz)**	4-12	11-14[A]	9-12
Acute/Chronic	Chronic	Acute[A]	Chronic
Progressive	Yes	No[A]	Yes
Alcohol	Effective	Effective	Effective
Tremor type	Action	Action	Action
Brain region	Cerebellum	Inferior olive[A]	Cerebellum

[A]Features different from human essential tremor patients are labelled red.

Table 2. **Cerebellar cell type expression patterns for five mouse cre driver lines.**

Mouse line	Stellate cells	Basket cells	Purkinje cells	CBN cells
PV^{cre}	Yes	Yes	Yes	Yes
L7^{cre}			Yes	
Prkcd^{cre}	Yes	Yes	Some	
Vglut2^{cre}				Glutermatergic
Gad2^{cre}	Yes	Yes	Yes	GABAergic